

Standing-Wave Transform Spectrometer Based on Integrated MEMS Mirror and Thin-Film Photodetector

Helen L. Kung, *Student Member, IEEE*, Sameer R. Bhalotra, *Student Member, IEEE*,
Justin D. Mansell, *Student Member, IEEE*, David A. B. Miller, *Fellow, IEEE*, and James S. Harris, Jr., *Fellow, IEEE*

Abstract—In this paper, we report a novel, miniature Fourier transform spectrometer with a linear architecture that works by sampling a standing wave. The spectrometer consists of an electrostatically actuated microelectromechanical mirror with on-resonance displacement of up to 65 μm , a thin-film photodetector, and an electrical back plane for actuating the mirror. The integrated device offers mirror stability and fixed relative alignment of the three components. The spectrometer has better than 32-nm resolution at 633 nm.

Index Terms—Fourier transform spectrometers, microelectromechanical devices, microsensors, spectral analysis, spectroscopy, wavelength measurement.

I. INTRODUCTION

MICROELECTROMECHANICAL systems (MEMS) technology has enabled the miniaturization of several types of spectrometers, including Fabry–Pérot interferometers [1], grating-based spectrometers [2], and Michelson spectrometers [3]. Of these designs, only the Michelson is a transform spectrometer. Transform spectrometers are useful for measuring both weak and broad spectra due to their fundamental multiplexing and throughput advantages. The multiplexing advantage arises because many frequencies of light are present at the detector at all times. This increases the detector signal-to-noise ratio during the recording of an interferogram. Here, we propose and demonstrate a new MEMS transform spectrometer that is based on sampling a standing wave in a linear architecture. This compact and thin spectrometer design avoids the beam splitting architecture and the consequent larger physical size of a Michelson interferometer.

A range of applications exists in which the compact size and simple operation of a MEMS transform spectrometer can outweigh its coarse spectral resolution. Such applications include biochemical analysis, mobile sensing systems, manufacturing line inspection, and vision systems [4]–[6]. The utility of such coarse spectrometers has been increased by simple signal pro-

cessing [7] that has enabled the real-time discrimination of different spectra. This simple processing also means that the operation of the spectrometer need not correspond exactly to the standard Fourier transform response, as long as the response of the spectrometer is linear in the signal; other forms of linear transform are usable. In the present spectrometer, this means that mirror scan need not be linear in time, allowing the use of a sinusoidal mirror scan. For the same reason, responses other than an ideal two-beam interference are also quite usable. In the present spectrometer, some Fabry–Pérot behavior can also be present, though again simple signal processing can deal with such effects.

Many devices based on sampling standing waves have been demonstrated. This class of devices has the advantage of surface normal design, which allows the possibility of combining many units in an array. One of us [8] first proposed a series of devices based on absorbers in a standing wave, ranging from wavelength monitors [9], [10] to laser tuners. Such structures have also been demonstrated as position sensors [11], and recently, we demonstrated a transform spectrometer [12] based on sampling a standing wave. In this paper, we will first describe the theory of a standing-wave spectrometer, then go into the components that were used to make our proof-of-principle integrated spectrometer, and finally conclude by comparing our spectrometer with a Michelson interferometer. This new design combines a MEMS mirror and a thin-film, semitransparent photodetector to make a 1.5-mm-thick spectrometer.

II. STANDING-WAVE SPECTROMETER THEORY

A standing wave is an interferogram that is generated by the superposition of forward and backward propagating waves. Fig. 1 shows a schematic diagram of a standing-wave spectrometer. We assume for a simplified first analysis that the system has low loss and no reflections off the detector interfaces. If the forward wave has an intensity of I_f , the backward wave has an intensity of I_b , the mirror is a perfect conductor, and the phase difference between the two waves is $\varphi = 2*2\pi\nu z/c + \pi$, for an optical frequency of ν , then the standing wave intensity at a particular point is

$$I(z) = I_f + I_b - 2\sqrt{I_f I_b} \cos\left(\frac{4\pi \nu z}{c}\right). \quad (1)$$

In our device, normally incident light is reflected from a mirror. The resulting backward propagating wave interferes

Manuscript received July 23, 2001; revised December 5, 2001. This work was supported in part by the United States Air Force Office of Scientific Research under Contract F49620-00-C-0040, and in part by the Defense Advanced Research Projects Agency under a grant for Photonic Wavelength And Spatial Signal Processing, under a Subcontract from FMA&H. The work of S. R. Bhalotra was supported by the Regina Casper Stanford Graduate Fellowship.

The authors are with the Departments of Electrical Engineering and Applied Physics, E. L. Ginzton and the Solid State and Photonics Laboratories, Stanford University, Stanford, CA 94305-4085 USA.

Publisher Item Identifier S 1077-260X(02)02235-9.

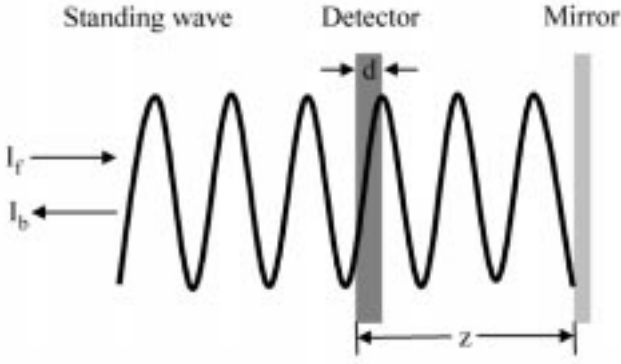


Fig. 1. Schematic of a standing-wave spectrometer and light intensity pattern where d is the thickness of the detector and z is the distance from the mirror to the detector.

with the forward propagating wave to generate a standing wave pattern. Using this type of architecture to generate the two interfering beams eliminates the need for a beam splitter. The forward propagating wave corresponds to the fixed arm of a Michelson interferometer, while the backward propagating wave corresponds to the arm with varying optical path length. As in the case of a Michelson, the input beam must be collimated with a maximum divergence angle [13] of

$$\theta = \sqrt{\frac{\lambda_{\min}}{2z_{\max}}} \quad (2)$$

where λ_{\min} is the smallest wavelength of interest and z_{\max} is the maximum distance between mirror and detector.

Displacement of the mirror causes the intensity of the standing wave at a given point to vary. A partially absorbing thin-film detector is placed at a fixed location to sample the standing wave as the mirror is translated. The detector signal at a given time is proportional to the integral of the optical intensity $I(z)$ over the thickness of the detector.

Equation (1) describes the interferogram for a monochromatic light source. To generalize it for a spectrum of light it is necessary to integrate over all frequencies. For simplicity here we assume that I_b is I_f attenuated by $e^{-\alpha d}$ in which α is the power absorption coefficient and d is the thickness of the detector. The interferogram $I(z)$ minus the constant optical intensities I_f and I_b is

$$I(z) - I_f - I_b = \int_0^{\infty} -2\sqrt{1 - e^{-\alpha d}} S_f(\nu) \cos\left(\frac{4\pi\nu z}{c}\right) d\nu \quad (3)$$

where S_f is the optical intensity spectrum of the incoming wave. If we assume $S_f(\nu)$ is an even function then it easily follows that $I(z) - I_b - I_f$ is proportional to the Fourier transform of $S_f(\nu)$. Sampling the standing wave the mirror moves is consequently equivalent to obtaining an interferogram using a Michelson spectrometer. We perform more sophisticated analysis, both algebraically below, and in more detailed calculations using transfer matrix methods [8], [14] in Section V, but the basic Fourier transform-like behavior is preserved as we do so.

There are tradeoffs between standing wave fringe visibility and detector thickness. To understand these tradeoffs better, we need to take into account the finite thickness and absorption of

the photodetector. We will make the following simplifying assumptions: 1) the mirror is a perfect conductor (i.e., mirror reflection causes a π phase shift); 2) the real index of refraction of the air gap and detector are the same or there is no reflection at the detector surfaces (which may be practically achieved by antireflection coating); and 3) the imaginary component of the electric susceptibility χ is small compared to the real component. With these assumptions, the magnitude of the incident backward wave is attenuated by passing through the detector with no phase shift due to the complex field reflection coefficient from the interfaces. With monochromatic electric fields of the form

$$E = E_0 \cos(2\pi\nu t) \quad (4)$$

the forward and backward spatial E -fields inside the detector are given by

$$E_{f0}(z) = E_{\text{inc}0} e^{-i(\beta - i(\alpha/2))z} \quad (5)$$

$$E_{b0}(z) = E_{\text{inc}0} e^{+i(\beta - i(\alpha/2))z} e^{-(\alpha/2)2d} e^{-i\varphi} \quad (6)$$

where $\beta = 2\pi n/\lambda$, λ is the optical wavelength, $E_{\text{inc}0}$ is the incident E -field, n is the real index of refraction and φ is the phase difference between the forward and backward waves including the phase shift off the mirror as given above.

The amount of power that is absorbed in the detector is equal to the time averaged rate-of-change of the work performed by the E -field on the detector's material. The power absorbed per unit volume is

$$W_{\text{abs}} = \left\langle E_{\text{tot}} \frac{\partial}{\partial t} P \right\rangle \quad (7)$$

where E_{tot} is the sum of forward and backward E -fields and P is the polarization. Only the imaginary portion of χ (absorption χ'') gives a nonzero term. Thus, the power absorbed per unit volume simplifies to

$$W_{\text{abs}}(z) = \frac{2\pi\nu\chi''\varepsilon_0}{2} |E_{f0}(z) + E_{b0}(z)|^2 \quad (8)$$

where ε_0 is the permittivity in air. This leads to a total power absorbed per unit area of

$$I_{\text{abs}} = \int_0^d W_{\text{abs}}(z) dz. \quad (9)$$

The incident power per unit area is equal to

$$I_{\text{inc}} = \frac{1}{2} \sqrt{\frac{\varepsilon_0}{\mu_0}} |E_{\text{inc}0}|^2. \quad (10)$$

where M_0 is the permeability in air. With $\alpha = 2\pi\nu\sqrt{\varepsilon_0\mu_0}\chi''$, the fractional power absorbed may therefore be calculated as

$$\begin{aligned} \frac{I_{\text{abs}}}{I_{\text{inc}}} &= \alpha \int_0^d \frac{|E_{f0}(z) + E_{b0}(z)|^2}{|E_{\text{inc}0}|^2} dz \\ &= \alpha \left[\frac{1 - \exp(-2\alpha d)}{\alpha} + \frac{\exp(-\alpha d)}{\beta} \right. \\ &\quad \left. \cdot (\sin(\varphi) - \sin(\varphi - 2\beta d)) \right] \\ &= \alpha \left[\frac{1 - \exp(-2\alpha d)}{\alpha} + \frac{\exp(-\alpha d)}{\beta} \right. \\ &\quad \left. \cdot (\sin(\varphi)(1 - \cos(2\beta d)) + \cos(\varphi) \sin(2\beta d)) \right]. \quad (11) \end{aligned}$$

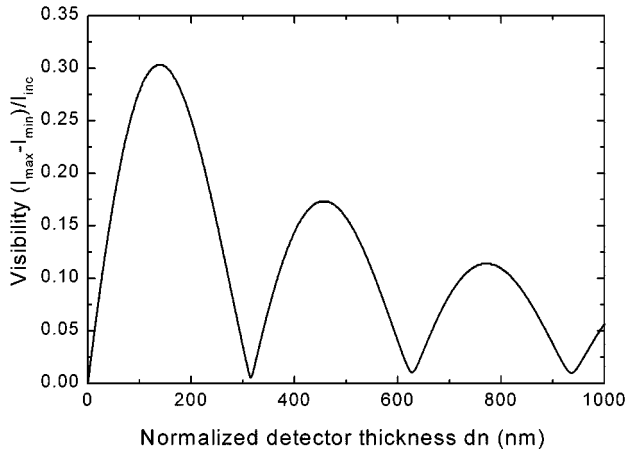


Fig. 2. Plot of visibility versus normalized detector thickness. $\alpha/n = 1000 \text{ cm}^{-1}$ and the thickness was plotted in units of dn , where n is the real part of the index of refraction.

To understand more clearly how this affects the visibility of the fringes, let us look more carefully at each term. Fringe visibility is conventionally defined as $(I_{\max} - I_{\min})/I_{\text{inc}}$, where I_{\max} and I_{\min} are the maximum and minimum absorbed intensities, respectively. The first term in the simplified version of (11) is a constant term independent of phase delay between the two beams. It represents the power absorbed through two passes of the detector. The second term is the interference term, which generates the fringes. For small α , maximum visibility occurs when $\cos(2\beta d) = -1$, which implies detector thickness of $(2m - 1)\lambda/4n$ where m is an integer. No visibility occurs when the $\cos(2\beta d) = 1$, which implies detector thickness of $m\lambda/2n$. The visibility versus detector thickness for $\lambda = 633 \text{ nm}$ and $\alpha/n = 1000 \text{ cm}^{-1}$ is shown in Fig. 2.

Note that the use of finite detector thickness will give a wavelength dependence to the visibility of fringes, again changing the spectrometer behavior compared to an ideal Fourier transform spectrometer. In general, this effect can again be taken care of by simple signal processing, though spectral features at specific frequencies (e.g., where the normalized detector thickness corresponds to integer numbers of half waves) could be completely suppressed, and this effect should be considered carefully if large spectral range is required.

For large α , (5) and (6) are no longer valid, because the assumption that the reflection off the detector interface is zero no longer holds even if the real refractive index is constant throughout or if a simple antireflection coating is applied to the detector. The reflection coefficient becomes a finite value. A full-fledged transfer matrix method [8], [13] is required to determine E_{f0} and E_{b0} . The modified E_{f0} and E_{b0} can be substituted into (11) to determine $I_{\text{abs}}/I_{\text{inc}}$. It is important to note, however, that even in the nonideal case of finite detector thickness and reflection, the standing-wave spectrometer still functions as a spectrometer, albeit with a spectral linear transform that differs from a simple Fourier transform. As mentioned before, simple signal processing [7] can deal with any particular linear transform to extract the desired information from the spectrum, especially when the goal is to recognize some spectral feature rather than make a scientific measurement of the conventional spectrum.

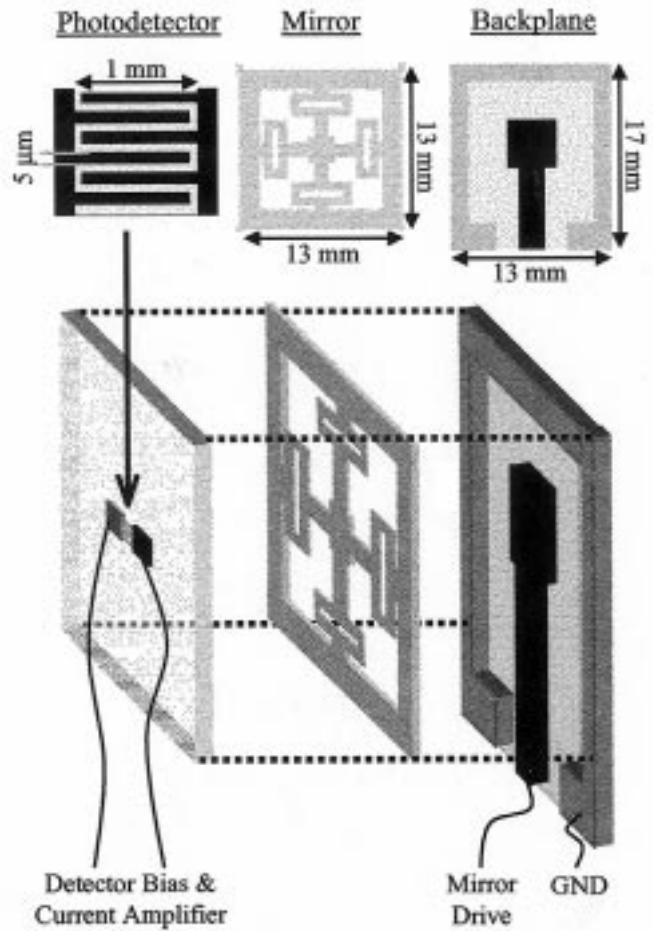


Fig. 3. Integrated standing-wave spectrometer.

III. SPECTROMETER DESIGN AND CONSTRUCTION

The standing-wave spectrometer uses two main components, a thin partially transparent fixed detector and a moving mirror. The fixed detector is used to sample the standing wave and the moving mirror is used to vary the standing wave's position. The $17 \times 13 \times 1.5$ -mm miniature standing-wave spectrometer was fabricated in separate planar components preceding integration, as shown schematically in Fig. 3.

An ideal spectrometer design includes a mirror with large displacement, moderate drive voltage, high load capacity, planar motion, and simple fabrication. Given these criteria, we chose an electrostatically actuated parallel-plate design with a large mirror surface operating in a sinusoidal mode for large displacement on resonance.

A. Mirror Design

Parallel-plate actuators are appropriate for moving a large mirror, which relaxes the optical alignment requirements and allows for larger beam sizes. The range of motion for typical parallel-plate actuator devices at moderate voltages is limited because their mirror membranes are supported in tension. We have developed an architecture that allows the support structures to bend rather than stretch. Fig. 4 shows a photograph of the front plane and a cross-sectional diagram of the mirror. On

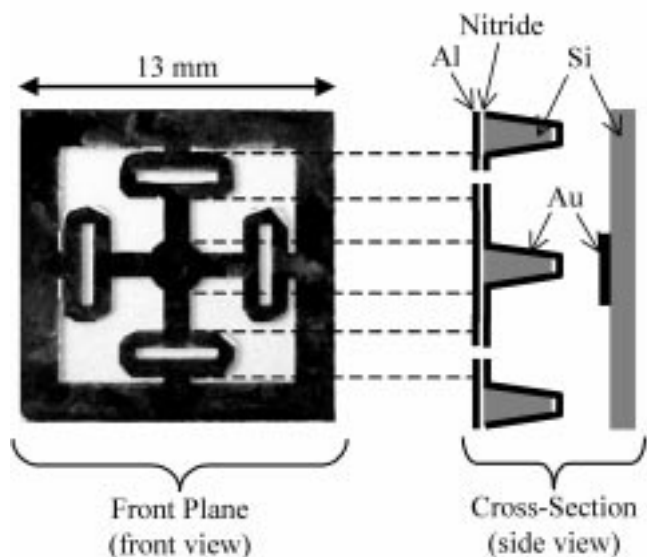


Fig. 4. Left: Photograph of the mirror front plane. Right: Side view schematic of mirror cross section. Aluminum, silicon nitride, silicon, and gold layers comprise the front plane. The back plane has a frame of gold and a gold electrode.

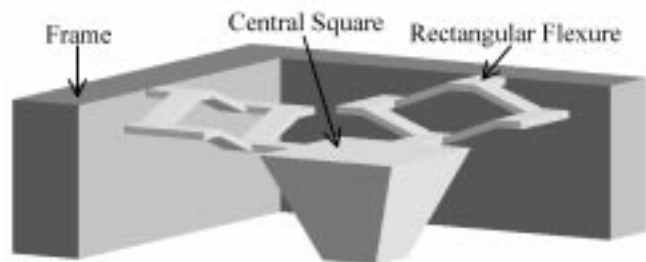


Fig. 5. Mirror front plane, depicting larger mirror motion. The rectangular flexures deform out of the plane, allowing the central square to move away from its equilibrium position.

the front plane, the inner square is the reflective surface, measuring 2 mm on a side; the sides of the outer square are 13 mm long. The four rectangular connecting flexures are the key to large displacement of the central square.

Fig. 5 shows the flexure deformation as the mirror is pulled down. The long side of each rectangular flexure bends. The stiffness of this structure is lower than that of a comparable structure built with support flexures in tension. This architecture decreases the effective spring constant, allowing for a larger range of motion.

To obtain large displacement the mirror was driven at resonance. Scan lengths of up to 65 μm have been demonstrated with this mirror actuator architecture [15]. Each rectangular flexure arm can be modeled as a linear flexure connecting the fixed outer frame to the reflective center square, as shown in Fig. 6. The spring constant k of each flexure is given by

$$k = \frac{Ewt^3}{L^3} \quad (12)$$

where E is the modulus of elasticity of the flexure material, w is the width of the arm (in the mirror plane), t is the thickness (normal to the plane), and L is the length. We ignore the thin

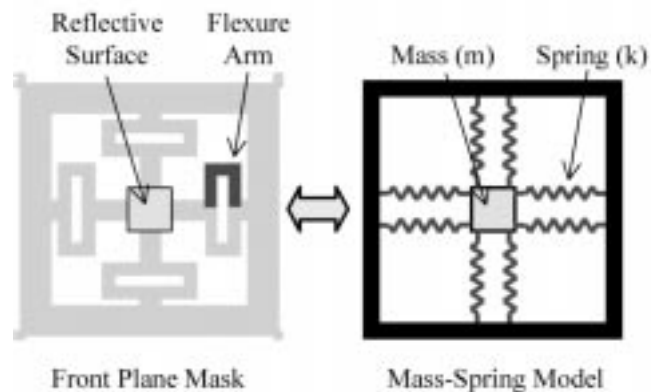


Fig. 6. Mechanical model of the mirror system. The eight flexure arms are represented by eight linear flexure springs in parallel.

nitride, gold, and aluminum layers, considering only the bulk Si; $E \sim 190$ GPa. A typical mirror has $w \sim 0.4$ mm, $t \sim 28$ μm , and $L \sim 5.9$ mm, and thus, $k \sim 8$ N/m. Including all eight flexures, the total $K \sim 60$ – 70 N/m. The large mass of the Si pillar behind the reflective center square $m \sim 2.8$ mg provides the inertia necessary for large motion on-resonance. The resonance frequency is given by

$$f = \frac{1}{2\pi} \sqrt{\frac{K}{m}}. \quad (13)$$

It is measured to be ~ 600 – 700 Hz. Slight variations in flexure dimensions are caused by variations in the wet etch rate and mask alignment to the silicon crystal planes during fabrication.

The resonance frequency is also temperature dependent, partially due to the temperature dependence of the silicon modulus of elasticity. We observe a change in measured resonance frequency of roughly 5% over a 10 $^\circ\text{C}$ ambient temperature range near room temperature. The resonance full-width at half-maximum (FWHM) is 100 Hz.

During initial efforts to fabricate long-throw MEMS mirrors for similar applications we implemented rectangular flexures with a lower aspect ratio and wider arms ($w \sim 1$ mm). To achieve the same desired resonance frequency of ~ 700 – 800 Hz, this necessitated a much smaller arm thickness ($t \sim 18$ – 20 μm), which increased the probability of mirror fracture in the fabrication process. The current design, with thicker flexure arms, significantly increases the yield.

Applying a voltage between the front and back planes causes the inner square on the front plane of the mirror to move because of electrostatic attraction. This is countered by the restoring force from the rectangular flexures. To determine the motion of the mirror, we solve the differential equation balancing the forces on the mirror front plane. The motion is described by

$$m \frac{\partial^2 z}{\partial t^2} + b \frac{\partial z}{\partial t} + Kz + \frac{V^2 \epsilon_0 A}{2(z_0 + z)^2} = 0 \quad (14)$$

with mirror displacement z measured from equilibrium. The first term is the acceleration with mass m . The second is the friction term where b is a general friction coefficient. Third is the first-order restoring force, with spring constant K . Last is the electrostatic force between two ideal parallel plates for voltage

V between the plates, common surface area A , and equilibrium separation distance z_o . ϵ_0 is the permittivity of free space. For a sinusoidal applied voltage with a dc offset, the solution to (14) is the motion of a driven, damped harmonic oscillator. Thus, the electrostatic driving force causes the mirror system to oscillate approximately sinusoidally at the driving frequency. For the mirror described above, with $z_o \sim 60 \mu\text{m}$ and mirror drive voltage $V_{pp} \sim 71 \text{ V}$, a total scan length of $13.7 \mu\text{m}$ was observed.

The measured motion is nearly sinusoidal with slight deviations due to the asymmetric electrostatic driving force. Thus, the displacement versus time is approximately

$$z(t) = \frac{S}{2} \cos(2\pi ft) \quad (15)$$

where f is the drive frequency, chosen to be the mechanical resonance frequency of the mirror actuator, and S is the scan length for a given drive voltage.

Structural asymmetry in the mirror front plane, including size or shape variations among the four rectangular flexures, can cause the reflective surface to deviate from parallel motion. This yields slight angular deflection of the reflected beam, which decreases the overlap of the forward and reflected beam, and thus, the amplitude of the standing wave sampled at the photodetector. Care during fabrication to align the wafer to the crystalline planes and a design that avoids extremely small flexure arms minimizes this effect.

To fabricate the mirror, we deposited $\sim 1 \mu\text{m}$ of low stress silicon nitride by low-pressure chemical vapor deposition (LPCVD) onto both sides of a double side polished $\langle 100 \rangle$ silicon wafer. The $500\text{-}\mu\text{m}$ -thick wafer was patterned with photoresist on the front using the mask pattern shown in Fig. 6. The back side was patterned with a mask containing only the frame and the central square. The nitride was then removed from the exposed areas by a plasma dry etch, after which the wafer was placed in a 75°C bath of 20% potassium hydroxide to etch the exposed silicon until $28 \mu\text{m}$ remained on the flexures. The electrode surface side of the wafer was coated with 100 \AA of chrome and then 2000 \AA of gold. The mirror surface was coated with 2000 \AA of aluminum for high reflectivity in the visible spectrum.

The mirror back plane was fabricated from an insulating quartz substrate. 100 \AA of chrome and 2000 \AA of gold were first deposited on the substrate. The metal layers were patterned, leaving a frame of gold to support the mirror front plane. The exposed quartz was then etched $60 \mu\text{m}$ with 6 : 1 buffered oxide etch (BOE), leaving space for mirror displacement. Finally, a center metal electrode was patterned to electrostatically attract the center pillar on the back of the mirror front plane.

B. Fixed Thin-Film Photodetector

The thin-film photodetector, mounted in front of the mirror front plane, must transmit a significant fraction of the input light to allow a standing wave of sufficient intensity. However, it must also absorb enough of the light to generate measurable photocurrent. Given the analysis in Section II and the material properties of silicon, the detector thickness was chosen to be $5\lambda/4n = 2200 \text{ \AA}$ at $\lambda = 633 \text{ nm}$. We chose to operate at the third peak in Fig. 2 instead of the first, because of the signifi-

cantly better quantum and collection efficiency of thicker detectors. The thicker detector decreases the ratio of surface area to volume, thus, making surface state effects less significant.

The detector was fabricated by LPCVD of 2200 \AA polysilicon on a quartz wafer at 620°C . The wafer was patterned with alternating fingers with a $5\text{-}\mu\text{m}$ spacing, and the 100 \AA of titanium, 300 \AA of nickel, and 2000 \AA of gold was lifted off. A $13 \times 13 \text{ mm}$ gold frame was patterned on the back side of the detector, and the quartz wafer was etched in 6 : 1 BOE to provide clearance for the mirror motion.

Polysilicon is used as the optically absorbing material. Ohmic metal–semiconductor contacts are used to extract photocurrent from the $1 \times 1 \text{ mm}$ active area. The thin-film detector has a -3 dB rolloff at 5 kHz , which diminishes the amplitude of the interference fringes at high frequencies. This places an upper bound on the useful mirror scan length and the spectral resolution of the device. For measurement of an interferogram with 40-kHz frequency components, the responsivity is $\sim 5 \mu\text{A/W}$ with 35-V applied bias. The responsivity of the detector could be improved by making the metal fingers with a transparent material and adding an antireflection coating to the detector surface.

In principle, any optically absorbing material can be used for the detector, thus allowing for different wavelength regimes and potentially better frequency response. The detector must either have a transparent substrate in the wavelength range of interest or the substrate may be removed and the detector bonded to a transparent substrate. Direct bandgap materials, such as GaAs or InP may have faster response and larger absorption coefficients than silicon.

C. Integrated Spectrometer Fabrication

The wafer planes were integrated by first electroplating $5 \mu\text{m}$ of indium on both the mirror back plane and the detector gold frame. The three components were then aligned with the mirror back plane on the bottom, the moving mirror in the middle, and the detector on the top. The wafer stack was heated to 190°C to melt the indium, and pressure was applied. Epoxy was applied around the edges of the integrated device to add mechanical strength. Electrical leads were soldered onto the two detector electrodes, the moving mirror electrode, and the back plane electrode. Finally, the integrated package was bonded with epoxy to a 1-in aluminum round for mounting in a standard optics mount. Fig. 7 shows the integrated spectrometer. This design has a spacer thickness of $490 \mu\text{m}$ and a maximum displacement of $\sim 13 \mu\text{m}$. This requires that the divergence angle of the input light be no more than 0.025 radians.

IV. EXPERIMENTAL RESULTS

The integrated mirror is actuated by applying a voltage between the back plane electrode and the gold-coated back of the mirror center square, while the frame is held fixed. The capacitance of this parallel-plate system is 2.6 pF . Driven with a dc-offset sinusoid on-resonance at 593 Hz with $V_{pp} \sim 71 \text{ V}$, the mirror moves harmonically with a total scan length of $13.7 \mu\text{m}$. The high scan rate enables continuous spectral analysis. The packaging helps dampen external vibrations that could couple to the moving mirror, and helps suppress the effect of air fluctuations. The packaging of all three planar components also guar-

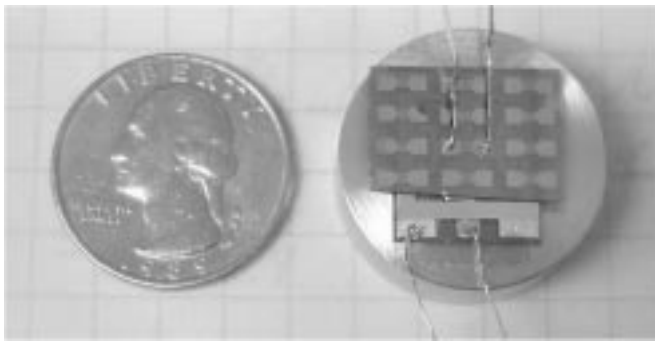


Fig. 7. The standing-wave spectrometer is shown mounted to a aluminum 1 in round. The three wafer planes are visible. The back plane is slightly larger than the mirror to allow for leads. The detectors were fabricated in arrays and the center one was used for the spectrometer.

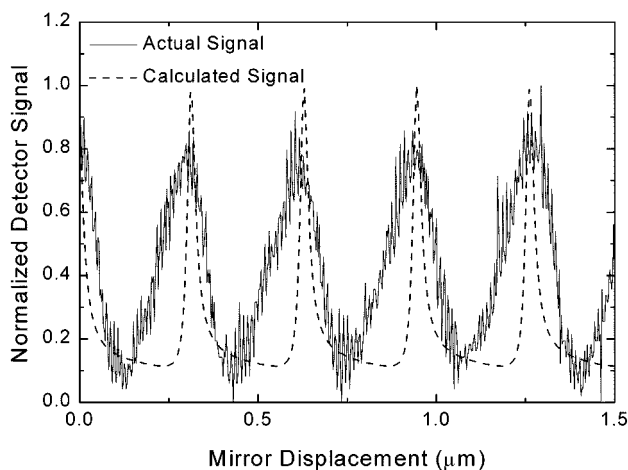


Fig. 8. The solid line is the measured data versus mirror displacement. The dashed lines are the graph of mirror displacement versus calculated standing-wave spectrometer dielectric stack.

antees alignment of the back plane electrode with the moving mirror center square, and more importantly, positional and angular alignment of the photodetector absorbing area with the moving mirror reflective surface.

The detector photocurrent is measured via a high-pass filter with -3 dB rolloff at 10 kHz to filter dc dark current and parasitic mirror drive feed-through noise. A low-noise current amplifier provides gain of 5×10^7 V/A, which is large enough to accommodate the signal attenuation due to interferogram frequencies well beyond the detector rolloff. The interferogram is sampled by a digital oscilloscope and transferred to a computer. The “current versus time” curve is mapped to a “current versus mirror displacement” curve, accounting for the nonlinear mirror motion. Finally, a discrete Fourier transform yields the optical spectrum.

The solid line in Fig. 8 shows the detector signal versus mirror displacement for a single wavelength (633 nm). The signal is not a pure sinusoid as would be expected from the interference equation of a standing wave. A transfer matrix method [8], [13] was used to model the dielectric stack that represents the detector, the air gap, and the aluminum mirror surface. A plot of the calculated detector signal versus mirror displacement is shown as a dotted line in Fig. 8. The graph resembles the

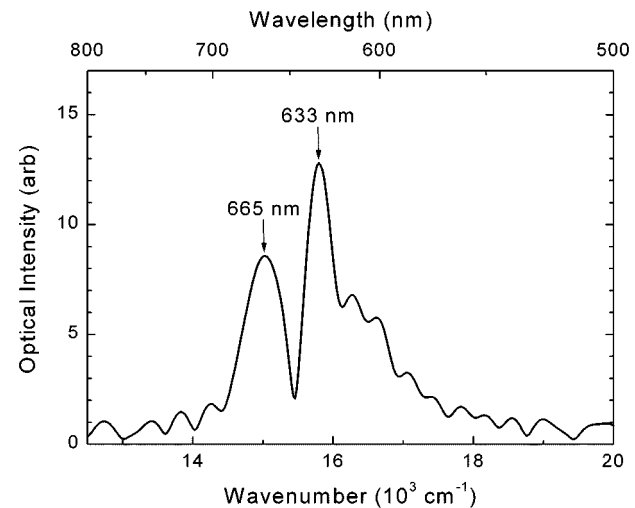


Fig. 9. Optical spectrum of 633 nm; 665-nm mixed spectrum.

case of a Fabry–Pérot cavity with a varying air gap because of the reflections off the polysilicon–air interface and the polysilicon–quartz interface. Also, in our device, there was a slight tilt between the detector and the mirror. This diminishes the Fabry–Pérot effect and the measured curve is quasi-sinusoidal. To approach the case of an ideal standing wave cavity, the detector must be antireflection coated on both sides to minimize the Fabry–Pérot effects and to get the full benefits of the multiplexing and throughput advantages. The finite frequency response of the detector will also tend to result in a more sinusoidal response with the detector unable to respond to the higher frequency components associated with the sharper Fabry–Pérot peaks. The absence of strong Fabry–Pérot effects in the actual recorded interferogram makes the response closer to that of a simple Fourier transform spectrometer.

Fig. 9 shows the spectrum calculated by taking the Fourier transform of an interferogram recorded as a function of mirror position for an input signal consisting of a combined laser diode beam (665 nm at $390 \mu\text{W}$) and HeNe beam (633 nm at $200 \mu\text{W}$). A significant portion of the diode laser power could not be coupled into the spectrometer because of the elliptical beam shape. The unequal peak heights in Fig. 9 correspond to different absorbed power levels. Using the 633-nm source to calibrate the spectrometer, the 665-nm source is correctly identified and well discriminated, yielding a spectral resolution of 32 nm, or 724 cm^{-1} . The FWHM of the 633-nm peak is 549 cm^{-1} and the FWHM of the 665 peak is 724 cm^{-1} . The two peaks are not the same width as would be expected for a fixed mirror displacement, because the two beams are not perfectly collinear. The widths of the peaks are greater than the width of the ideal sinc function and the side lobes are smaller, because the nonparallel motion of the mirror causes an apodization of the standing wave signal.

V. COMPARISON TO MICHELSON INTERFEROMETER

A standing-wave spectrometer differs fundamentally from a Michelson interferometer in two respects. First, the ability to measure spectra of low coherence length light is limited by the minimum distance that can be achieved between the mirror and

the detector. Second, the detector is only partially absorbing, which leads to a tradeoff between fringe visibility and the wavelength-multiplexing figure of merit.

The minimum distance that can be achieved between the detector and the mirror determines the lowest coherence length light that can be measured. Hence, the distance between the mirror and the detector can be engineered to suppress unwanted low coherence length light. In our spectrometer design the minimum distance between the detector and the mirror is $\sim 490 \mu\text{m}$ at the point of closest approach. This is similar to a Michelson with arms that differ in length by a minimum of $\sim 490 \mu\text{m}$. Therefore, spectral components with coherence lengths less than $980 \mu\text{m}$ are not resolved. This corresponds to only resolving spectral components with $\Delta\nu < 3 \times 10^{11} \text{ Hz}$ (10 cm^{-1}) or $\Delta\lambda < 0.4 \text{ nm}$ at 633 nm . This design tradeoff is not significant for applications involving the detection of sharp spectral features. Decreasing the initial distance between the mirror and detector would allow detection of light with lower coherence length.

The second tradeoff is more complex and is a consequence of the partially absorbing thin detector. If the detector absorbs all the light on the first pass, no standing wave is created. On the other hand, if very little light is absorbed, the detector signal strength becomes unacceptably weak.

To understand the consequences of this tradeoff, a rigorous transfer matrix method [8], [13] was used to explore the fundamental limits of the standing-wave spectrometer. To represent an ideal case, we assume, first of all, that the real index of refraction is constant everywhere in the device ($n = 3.5$). For the purposes of this analysis, this is equivalent to assuming that perfect $\lambda/4$ antireflection coatings are applied to the detector surfaces. Second, the detector is assumed to be the only lossy element in the system. Finally, we performed our calculations at $\lambda = 633 \text{ nm}$.

To compare the standing-wave spectrometer to a Michelson we define two figures of merit. The first is the fringe visibility $V = (I_{\text{max}} - I_{\text{min}})/I_{\text{inc}}$. In the Michelson case, $V = 1$. The second figure of merit M characterizes the wavelength-multiplexing advantage of the standing wave design. It is proportional to the fraction of incident photons that contribute to usable detector signal during one scanning period. This figure of merit is equal to the area under the interferogram, given by

$$\frac{1}{L} \int_0^L \frac{I(z) - I_{\text{min}}}{I_{\text{inc}}} dz \quad (16)$$

where $L = \lambda/(2n)$ is one period of the monochromatic interferogram. In a Michelson interferometer, the fringes are sinusoidal, so $M = 1/2$.

Fig. 10 (right axis) shows the detector thickness required to optimize the fringe visibility for a given absorption coefficient α . For small absorption, the optimal detector thickness is $\lambda/4n$. As α increases the optimum detector thickness decreases. The left axis shows the figures of merit V (visibility) and M for the optimized detector thickness versus absorption coefficient. As shown in the figure, it is possible to achieve a fringe visibility of one for large α . However, this result is only due to Fabry-Pérot

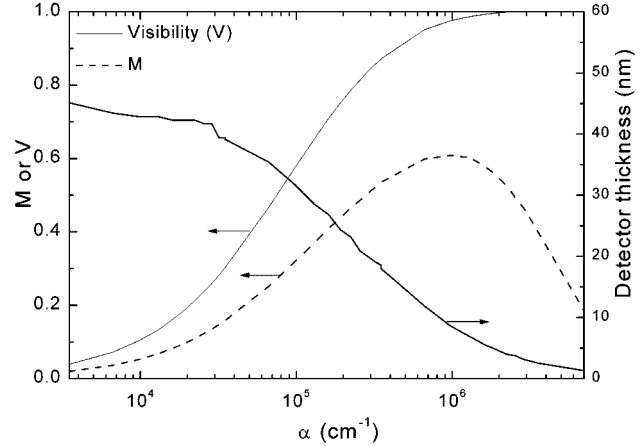


Fig. 10. Figures of merit, V and M (left axis), and optimal detector thickness (right axis) versus power absorption coefficient.

effects. Complex phase shifts at the detector from reflections that cannot be ignored.

Fabry-Pérot spectrometers do not offer the wavelength-multiplexing advantage of the standing wave design. At each particular mirror spacing, there is only one narrow frequency range that is absorbed by the detector. Thus, for a Fabry-Pérot filter, M is small, which contributes to the fall of M for large absorption coefficients in Fig. 10.

The peak value $M \sim 0.6$ occurs at $\alpha \sim 10^6 \text{ cm}^{-1}$ where the visibility V is 96%. This operating point corresponds to a single-pass power absorption of 60%. The visibility is slightly less than that of a Michelson, but M is greater. This is because the detector signal versus mirror displacement curve has the form $\cos^2(z)$ for small complex reflections. In practice, it is difficult to find materials that have $\alpha \sim 10^6 \text{ cm}^{-1}$, so it is necessary to settle for smaller fringe visibility and M .

The area underneath the interferogram only partially describes the wavelength-multiplexing advantage of the standing-wave spectrometer, because the optimum detector thickness is frequency dependent. These calculations show, that compared to a Michelson interferometer, there is no major tradeoff in a standing-wave spectrometer, except the inherent nonuniform wavelength response. In practice, with antireflection coated detector surfaces and an absorbing material where $\alpha \sim 10^5 \text{ cm}^{-1}$ it would be possible to have $V \sim 65\%$ and $M \sim 38\%$.

VI. CONCLUSION

We have demonstrated a miniaturized spectrometer using a linear architecture that permits many individual units to be laid out in a two-dimensional array format, allowing the possibility of an imaging array of spectrometers. Our integrated standing-wave spectrometer obtained 32-nm resolution at $\lambda = 665 \text{ nm}$. This compact, stable design is composed of three planar components that can be separately fabricated with different materials, in principle accommodating any wavelength range of interest. We have also shown that it should be possible to design the standing-wave spectrometer, so that its efficiency is comparable to that of a Michelson spectrometer.

REFERENCES

- [1] P. M. Zavracky, K. L. Denis, H. K. Xie, T. Wester, and P. Kelley, "A micromachined scanning Fabry-Pérot interferometer," *Proc. SPIE*, vol. 3514, pp. 179–187, 1998.
- [2] G. M. Yee, N. I. Maluf, P. A. Hing, M. Albin, and G. T. A. Kovacs, "Miniature spectrometers for biochemical analysis," *Sensors and Actuators A—Physical*, vol. A58, pp. 61–66, Jan. 1997.
- [3] O. Manzardo, H. P. Herzig, C. R. Marxer, and N. F. de Rooij, "Miniaturized time-scanning Fourier transform spectrometer based on silicon technology," *Opt. Lett.*, vol. 24, pp. 1705–1707, Dec. 1999.
- [4] J. H. Correia, G. de Graaf, S. H. Kong, M. Bartek, and R. F. Woffenbuttel, "Single-chip CMOS optical microspectrometer," *Sensors and Actuators A—Physical*, vol. A82, pp. 191–197, May 2000.
- [5] R. J. McNichols and G. L. Cote, "Optical glucose sensing in biological fluids: An overview," *J. Biomedical Opt.*, vol. 5, pp. 5–16, Jan. 2000.
- [6] S. D. Brown, "Real-time filtering of data from mobile, passive remote infrared sensors with principal component models of background," *J. Chemometrics*, vol. 5, pp. 147–161, May 1991.
- [7] S. R. Bhalotra, H. L. Kung, and D. A. B. Miller, "Real-time discrimination of spectra by time-domain adaptive filtering in a Fourier transform interferometer," in *Proc. Conf. Fourier Transform Spectroscopy*, 2001, pp. PD 2-1–PD 2-3.
- [8] D. A. B. Miller, "Laser tuners and wavelength sensitive detectors based on absorbers in standing waves," *IEEE J. Quantum Electron.*, vol. 33, pp. 732–749, Mar. 1994.
- [9] H. L. Kung, D. A. B. Miller, P. Atanackovic, C. C. Lin, J. S. Harris, Jr., L. Carraresi, J. E. Cuningham, and W. Y. Jan, "Wavelength monitor based on two single quantum well absorbers sampling a standing wave pattern," *Appl. Phys. Lett.*, vol. 76, pp. 3185–3187, May 2000.
- [10] G. Masini, L. Colace, and G. Assanto, "Near infrared wavemeter based on an array of polycrystalline Ge on Si photodetectors," *Proc. SPIE*, vol. 3953, pp. 88–94, 2000.
- [11] M. Sasaki, X. Mi, and K. Hane, "Ultra-thin film photodiodes for use in position sensors," *J. Modern Opt.*, vol. 48, pp. 55–66, Jan. 2001.
- [12] H. L. Kung, S. R. Bhalotra, J. D. Mansell, and D. A. B. Miller, "Compact transform spectrometer based on sampling a standing wave," in *Proc. International Conf. Optical MEMS*, 2000, pp. 19–20.
- [13] J. Chamberlain, *The Principles of Interferometric Spectroscopy*. New York: Wiley, 1979, pp. 216–221.
- [14] H. A. Macleod, *Thin-Film Optical Filters*, 2nd ed. New York: McGraw-Hill, 1989, pp. 32–51.
- [15] S. R. Bhalotra, J. D. Mansell, H. L. Kung, and D. A. B. Miller, "Parallel-plate MEMS mirror design for large on-resonance displacement," in *Proc. Int. Conf. Optical MEMS*, 2000, pp. 93–94.



Helen L. Kung (S'99) received the B.S. degree in electrical engineering from Brown University and the M.S. degree in electrical engineering from Stanford University in 1996 and 1997, respectively. She is presently working toward the Ph.D. degree in electrical engineering under Prof. David A. B. Miller at Stanford University, where her research involves miniaturized optical spectral sensors.



Sameer R. Bhalotra (S'01) was born in Derby, CT, on July 8, 1976. He received the A.B. degree in chemistry and physics from Harvard University, and the M.S. degree in applied physics from Stanford University in 1998 and 2001, respectively. He is currently working toward the Ph.D. degree in applied physics under Prof. David A. B. Miller at Stanford University, where his research involves the development of miniaturized optical sensing systems.



Justin D. Mansell (S'95) received his B.S. and M.S. degrees in electrical engineering and applied physics from Case Western Reserve University, Cleveland, OH, in 1996 and defended his Ph.D. at Stanford University in 2001.

He founded Intellite, Inc., Albuquerque, NM, in 2001 with his father, Dennis Mansell. His work at Intellite is concentrated on commercializing the micromachined active mirror technology. He has been awarded several patents for his work on Hartmann sensing, microoptics, and micromachined

deformable mirrors.

Dr. Mansell is a member of the Optical Society of America (OSA) and the Society of Photo-optical Instrumentation Engineers (SPIE).



David A. B. Miller (M'84–SM'89–F'95) received the B.Sc. degree from St. Andrews University, and the Ph. D. degree from Heriot-Watt University, in 1979.

He was with Bell Laboratories, from 1981 to 1996, as a Department Head from 1987, latterly of the Advanced Photonics Research Department. He is currently the W. M. Keck Foundation Professor of Electrical Engineering at Stanford University, Stanford, CA, and Director of the Ginzton and Solid State and Photonics Laboratories, Stanford, CA. His research

interests include quantum-well optoelectronic physics and devices, and fundamentals and applications of optics in information, sensing, switching, and processing. He has published more than 200 scientific papers, and holds over 40 patents.

Dr. Miller has served as a Board member for both the Optical Society of America (OSA) and IEEE Lasers and Electro-Optics Society (LEOS), and in various other society and conference committees. He was President of the IEEE Lasers and Electro-Optics Society in 1995. He was awarded the Adolph Lomb Medal and R. W. Wood Prize from the OSA, the International Prize in Optics from the International Commission for Optics, and an IEEE Third Millennium Medal. He is a Fellow of the Royal Society of London, OSA, and APS, and holds an honorary degree from the Vrije Universiteit Brussel.



James S. Harris, Jr. (F'88) received the B.S., M.S., and Ph.D. degrees in electrical engineering from Stanford University, Stanford, CA, in 1964, 1965, and 1969, respectively.

He is the James and Ellenor Chesebrough Professor of Engineering at Stanford University. In 1969, he joined the Rockwell International Science Center, Thousand Oaks, CA, where he was one of the key contributors in developing their preeminent position in GaAs device technology. In 1982, he joined the Solid State Electronics Laboratory, Stanford University, as Professor of Electrical Engineering. He served as Director of the Solid State Electronics Laboratory at Stanford University from 1981 to 1988. His current research interests are in the physics and application of ultra-small structures to new electronic and optoelectronic devices and high-speed integrated circuits and MBE growth coupled with a scanning-probed-induced oxidation for fabrication of nano three-dimensional structures. He has more than 500 publications in these areas.

Dr. Harris, Jr. is a Fellow of the American Physical Society and he received the Heinrich Walker medal, IEEE Third Millennium Medal, and the 2000 IEEE Morris N. Liebmann Memorial Award for his contributions to GaAs devices and technology.